

## **New Generation Hole Transporting Materials for Perovskite Solar Cells Amide-Based Small-Molecules with Nonconjugated Backbones**

Petrus, Michiel L.; Schutt, Kelly; Sirtl, Maximilian T.; Hutter, Eline M.; Closs, Anna C.; Ball, James M.; Bijleveld, Johan C.; Petrozza, Annamaria; Bein, Thomas; Dingemans, Theo J.

**DOI**

[10.1002/aenm.201801605](https://doi.org/10.1002/aenm.201801605)

**Publication date**

2018

**Document Version**

Final published version

**Published in**

Advanced Energy Materials

**Citation (APA)**

Petrus, M. L., Schutt, K., Sirtl, M. T., Hutter, E. M., Closs, A. C., Ball, J. M., Bijleveld, J. C., Petrozza, A., Bein, T., Dingemans, T. J., Savenije, T. J., Snaith, H., & Docampo, P. (2018). New Generation Hole Transporting Materials for Perovskite Solar Cells: Amide-Based Small-Molecules with Nonconjugated Backbones. *Advanced Energy Materials*, 18(32), Article 1801605. <https://doi.org/10.1002/aenm.201801605>

**Important note**

To cite this publication, please use the final published version (if applicable).  
Please check the document version above.

**Copyright**

Other than for strictly personal use, it is not permitted to download, forward or distribute the text or part of it, without the consent of the author(s) and/or copyright holder(s), unless the work is under an open content license such as Creative Commons.

**Takedown policy**

Please contact us and provide details if you believe this document breaches copyrights.  
We will remove access to the work immediately and investigate your claim.



# New Generation Hole Transporting Materials for Perovskite Solar Cells: Amide-Based Small-Molecules with Nonconjugated Backbones

Michiel L. Petrus,\* Kelly Schutt, Maximilian T. Sirtl, Eline M. Hutter, Anna C. Closs, James M. Ball, Johan C. Bijleveld, Annamaria Petrozza, Thomas Bein, Theo J. Dingemans, Tom J. Savenije, Henry Snaith, and Pablo Docampo\*

State-of-the-art perovskite-based solar cells employ expensive, organic hole transporting materials (HTMs) such as Spiro-OMeTAD that, in turn, limits the commercialization of this promising technology. Herein an HTM (EDOT-Amide-TPA) is reported in which a functional amide-based backbone is introduced, which allows this material to be synthesized in a simple condensation reaction with an estimated cost of  $< \$5 \text{ g}^{-1}$ . When employed in perovskite solar cells, EDOT-Amide-TPA demonstrates stabilized power conversion efficiencies up to 20.0% and reproducibly outperforms Spiro-OMeTAD in direct comparisons. Time resolved microwave conductivity measurements indicate that the observed improvement originates from a faster hole injection rate from the perovskite to EDOT-Amide-TPA. Additionally, the devices exhibit an improved lifetime, which is assigned to the coordination of the amide bond to the Li-additive, offering a novel strategy to hamper the migration of additives. It is shown that, despite the lack of a conjugated backbone, the amide-based HTM can outperform state-of-the-art HTMs at a fraction of the cost, thereby providing a novel set of design strategies to develop new, low-cost HTMs.

with outstanding optoelectronic properties.<sup>[1]</sup> In 2009, these materials were introduced in solar cells and have since established a striking increase in performance, reaching over 22% in state-of-the-art devices.<sup>[2]</sup> Here, the perovskite absorber is sandwiched between two selective charge extraction layers, that transport the charges to the electrodes.<sup>[3]</sup> Although efficient inorganic hole transporting materials (HTMs) have been reported,<sup>[4]</sup> the most well-known HTMs are the organic materials 2,2',7,7'-tetrakis-(*N,N*-di-4-methoxyphenylamino)-9,9'-spirobifluorene (Spiro-OMeTAD) and polytriarylamine (PTAA). Alternatives that compete in performance have been published,<sup>[5–7]</sup> however, just like Spiro-OMeTAD and PTAA, most of these materials are synthesized in multistep synthetic procedures, involving (transition) metal catalyzed cross-coupling reactions,

## 1. Introduction

Hybrid metal halide perovskites have attracted enormous attention due to their simple preparation in combination

stringent reaction conditions and extensive product purification. This results in a relative high material cost, consequently leading to a significant contribution to the total device cost.<sup>[5,8,9]</sup> Additionally, the tedious synthesis hampers large

Dr. M. L. Petrus, M. T. Sirtl, A. C. Closs, Prof. T. Bein  
Department of Chemistry and Center for NanoScience (CeNS)  
University of Munich (LMU)  
Butenandtstr. 11, 81377 Munich, Germany  
E-mail: michiel.petrus@cup.lmu.de, michiel.petrus@gmail.com

K. Schutt, Prof. H. Snaith  
Clarendon Laboratory  
Department of Physics  
University of Oxford  
Parks Road, Oxford OX1 3PU, UK

Dr. E. M. Hutter, Dr. T. J. Savenije  
Department of Chemical Engineering  
Delft University of Technology  
van der Maasweg 9, 2629 HZ Delft, The Netherlands

The ORCID identification number(s) for the author(s) of this article can be found under <https://doi.org/10.1002/aenm.201801605>.

DOI: 10.1002/aenm.201801605

Dr. J. M. Ball, Dr. A. Petrozza  
Center for Nano Science and Technology@Polimi  
Istituto Italiano di Tecnologia  
via, Giovanni Pascoli 70/3, 20133 Milan, Italy

Dr. J. C. Bijleveld  
Faculty of Aerospace Engineering  
Delft University of Technology  
Kluyverweg 1, 2629 HS Delft, The Netherlands

Prof. T. J. Dingemans  
Department of Applied Physical Sciences  
University of North Carolina at Chapel Hill  
Murray Hall 1113, 121 South Road  
Chapel Hill, NC 27599-3050, USA

Dr. P. Docampo  
Newcastle University  
School of Electrical and Electronic Engineering  
NE1 7RU Newcastle upon Tyne, UK  
E-mail: pablo.docampo@newcastle.ac.uk

scale production of these materials and thereby could impede the commercial success of perovskite solar cells.

In contrast, our recently introduced approach using condensation chemistry has proven its value as a low-cost and easily scalable chemistry to prepare organic HTMs for perovskite solar cells.<sup>[10–12]</sup> More importantly, no expensive metal catalysts are required when using this chemistry, the synthesis can be done at ambient conditions and since water is the only side-product, product purification is very straightforward.<sup>[13]</sup> Azomethine-, enamine-, and hydrazone-based organic molecules have been reported as HTMs, although none of these materials have been able to outperform state-of-the-art materials.<sup>[10,12,14,15]</sup>

Aromatic amides can also be synthesized using simple condensation chemistry and are well-known as building blocks for high-performance polymers with outstanding chemical and thermal stability. Kevlar is perhaps the most well-known example and owes its unique properties to a high backbone rigidity and strong intermolecular hydrogen bonding interactions. Nonetheless, as the amide-bond is not conjugated, it is generally believed to be a poor linker for the preparation of semiconducting materials, as it is postulated to hamper charge transport.<sup>[16]</sup> However, poor intramolecular charge transport may be overcome via enhanced intermolecular interactions in bulk materials. For instance, favorable hydrogen bonding can promote close molecular packing and good intermolecular orbital overlap, leading to enhanced charge transport properties.<sup>[17]</sup> For this reason we believe that aromatic amide-based HTMs have been overlooked and that their great potential remains untapped.

In this work, we introduce a simple HTM (EDOT-Amide-TPA) based on well-known building blocks, which are linked together via amide functionalities, demonstrating the first HTM for perovskite solar cells with an amide-based backbone. For a

nonconjugated material, this HTM shows outstanding charge carrier properties that can compete with conjugated HTMs used in the current generation of state-of-the-art perovskite solar cells. Based on these results, we demonstrate that conjugation through the backbone is not essential in order to obtain materials with good charge transporting properties. The amide-bonds in EDOT-Amide-TPA have the ability to coordinate with Li-ions, and we hypothesize that this limits the migration of Li-containing additives, resulting in an improved device stability.<sup>[18]</sup> We studied the charge transfer dynamics at the perovskite/HTM interface via time-resolved microwave conductivity (TRMC) measurements, revealing that our EDOT-Amide-TPA HTM efficiently extracts holes from the perovskite faster than Spiro-OMeTAD. We employed EDOT-Amide-TPA in perovskite solar cells and obtained devices with power conversion efficiencies (PCEs) exceeding 20%. We additionally compare the performance, robustness and stability of these devices with those comprising current state-of-the-art Spiro-OMeTAD. Our amide-based EDOT-Amide-TPA outperforms Spiro-OMeTAD in all categories at a fraction of the cost (5%), which makes this a breakthrough and a key development in the design of future low-cost HTMs.

## 2. Synthesis

The production of amide-based materials has proven its value in industry, as these materials can be made using straightforward chemistry with excellent yields and high purity. We use these aromatic amides as building blocks for the preparation of a semiconducting small-molecule termed “EDOT-Amide-TPA” (Figure 1a; Figures S1 and S2, Supporting Information), which was prepared by condensing 4-amino-4',4'',-dimethoxytriphenylamine

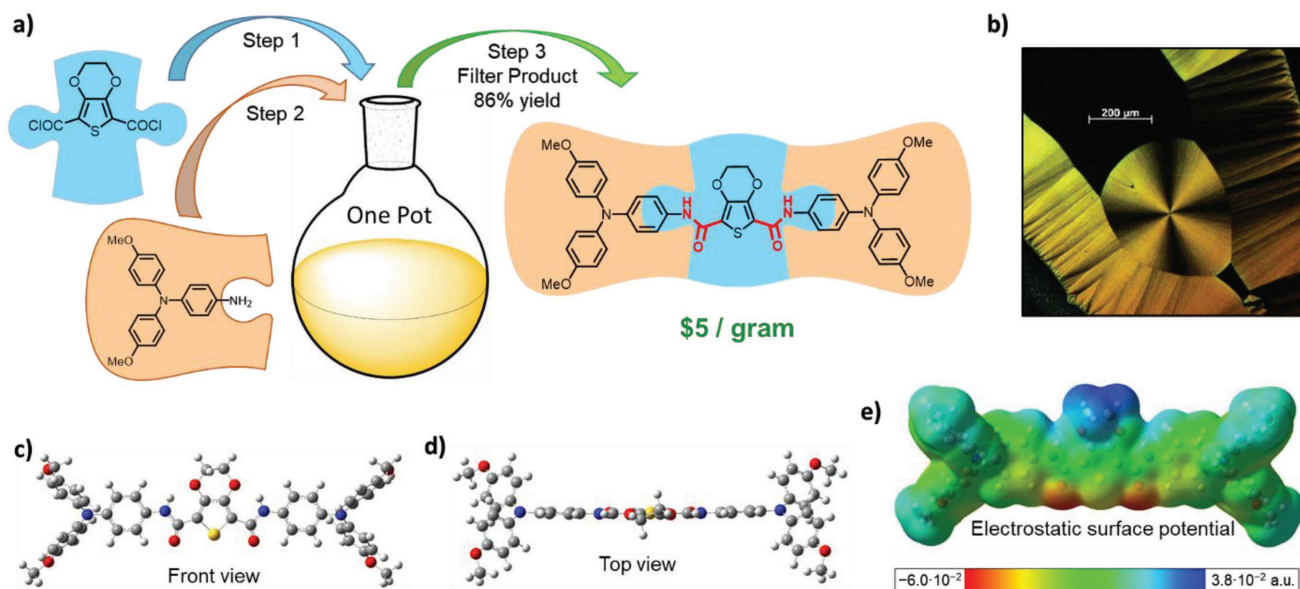


**Figure 1.** Structure of EDOT-Amide-TPA. a) One-pot reaction scheme and molecular structure of EDOT-Amide-TPA and its starting materials, where the amide bond in the product is highlighted in red. b) Microphotographs (crossed polars 10×) of EDOT-Amide-TPA crystallized from the melt at 168 °C. c,d) Optimized geometry obtained from DFT calculation, displaying the planar core. e) Electrostatic surface potential map, revealing the strong dipole in the core.

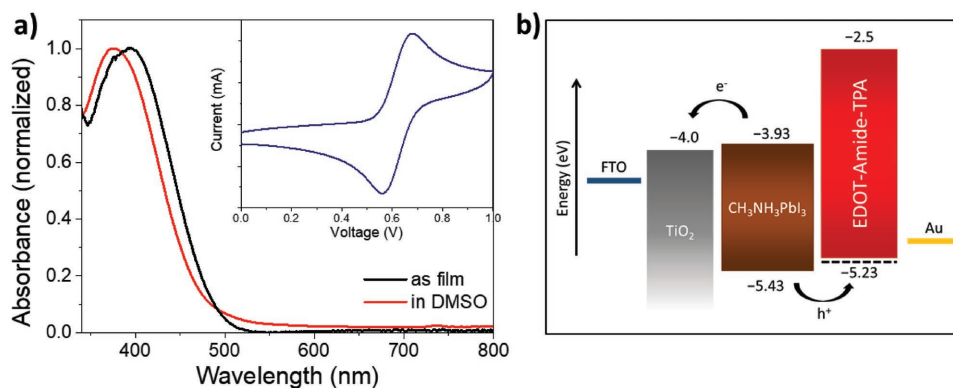


**Figure 2.** Optoelectronic properties of EDOT-Amide-TPA. a) Normalized UV-vis absorption profile of EDOT-Amide-TPA in DMSO and as a thin film; the inset shows the cyclic voltammogram of EDOT-Amide-TPA measured in a dichloromethane solution containing tBuNPF<sub>6</sub> as electrolyte. Oxidation potential is measured versus Ag/Ag<sup>+</sup>. b) Energy level diagram showing the energy levels for EDOT-Amide-TPA obtained from cyclic voltammetry and UV-vis measurements. The dotted line shows the HOMO energy level obtained from computational studies.

(3) with 2,3-dihydrothieno[3,4-b][1,4]dioxine-5,7-dihydrochloric acid (2) in the presence of a base in a simple one-pot reaction. During the reaction the product precipitates, making the workup very straightforward, as only a simple washing step is required for purification. This results in a good isolated yield of 86% and very high purity, while the simplicity of the chemistry reduces batch-to-batch variations.

In order to give an estimate of the materials cost, we performed a cost-analysis following published procedures based on lab scale synthesis (Figure S4 and Table S1, Supporting Information).<sup>[10,19]</sup> We obtained an estimated materials cost of only 5 \$ g<sup>-1</sup>, which is more than an order of magnitude lower than the estimated materials cost of Spiro-OMeTAD (92 \$ g<sup>-1</sup>) and also significantly lower than other high performing organic HTMs.<sup>[5,10,20,21]</sup> Additionally, EDOT-Amide-TPA can be synthesized without the use of halogenated solvents at only a slightly higher cost, which is essential for industrial production as many halogenated solvents have been banned from industrial processes.<sup>[22]</sup>

### 3. Characterization

Aromatic amides are well-known for their outstanding thermal and chemical stability.<sup>[23]</sup> This is of importance for photovoltaic devices, as the HTM should not degrade under full operational conditions, which can reach over 80 °C. Thermogravimetric analysis (TGA) confirms the excellent thermal stability of EDOT-Amide-TPA with a degradation temperature close to 350 °C (Figure S5, Supporting Information). Differential scanning calorimetry (DSC) measurements expose the polymorph character of EDOT-Amide-TPA (Figure 1b; Figure S6, Supporting Information), which was confirmed by X-ray diffraction measurements (Figure S7, Supporting Information). The material has two different melting transitions, depending on the crystal structure, at 237 and 275 °C and a glass-transition temperature ( $T_g$ ) at 112 °C. Additionally, a cold crystallization at 180 °C was observed. All thermal transitions exceed the general operation temperature of photovoltaic devices and are also higher than the thermal transitions of its conjugated analogues (Table S2, Supporting Information).

In order to estimate the bandgap of EDOT-Amide-TPA, light absorption measurements were performed (Figure 2a). The solvent has an influence on the absorption spectra, as protic and basic solvents can interact with the amide-bond. The rather comparable optical absorption spectra obtained from solution and as a thin film suggests that the EDOT-Amide-TPA film is in an amorphous state, which is in agreement with the lack of reflections in X-ray diffraction (XRD) measurements. The films show an absorption maximum at 395 nm and the absorption onset of the film was determined by a Tauc plot to be 485 nm, corresponding to an optical bandgap of 2.7 eV.

A good energy alignment between the perovskite absorber and the HTM is important to minimize losses in photovoltaic devices. The oxidation potential of EDOT-Amide-TPA was determined using cyclic voltammetry, from which the highest occupied molecular orbital (HOMO) energy level was calculated (Figure 2a, inset).<sup>[10]</sup> We observe a reversible oxidation with an onset at 0.53 V versus Ag/Ag<sup>+</sup>, resulting in a HOMO energy level of -5.23 eV, which is 100 meV deeper than that of Spiro-OMeTAD (Figure S8, Supporting Information). The lowest unoccupied molecular orbital (LUMO) energy level was estimated to be -2.5 eV, obtained by adding the optical bandgap to the HOMO energy level. The HOMO energy level matches well with the valence band of the perovskite and is expected to result in minimal losses in the open-circuit voltage ( $V_{oc}$ ), while the high LUMO energy level allows EDOT-Amide-TPA to function as an efficient electron blocking layer (Figure 2b).

### 4. Molecular Geometry Simulations

Computational studies were performed to gain insight into the geometry and electronic structure of EDOT-Amide-TPA. Density functional theory (DFT) geometry optimizations were performed and the optimized geometry shows that the amide bond and the aromatic core of the molecule are all in a single plane, allowing for close molecular packing of the small-molecules (Figure 1c,d). The methoxy-containing phenyl rings of the triphenylamines are twisted out-of-plane, promoting the solubility of the small-molecule. The HOMO is concentrated over the triphenylamine side groups (Figure S9,

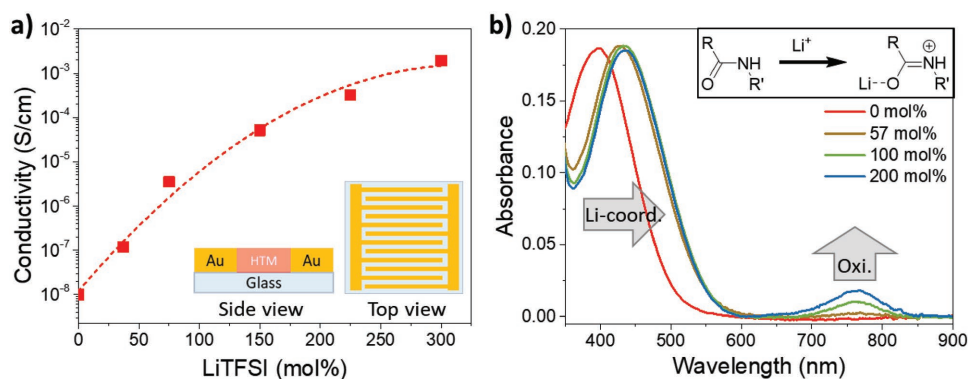


**Figure 3.** Charge transporting properties of EDOT-Amide-TPA. a) The measured electrical conductivity as a function of the amount of LiTFSI added to the solution used for spincoating the films. The dotted line is added as a guide to the eye. The inset shows a schematic representation of the interdigitated electrode pattern on the device. b) UV-vis absorption spectra of EDOT-Amide-TPA films as a function of added LiTFSI. The UV-vis spectra show the formation of the oxidized species in the range of 700–800 nm and a red-shift in the absorption maximum (400–440 nm) of the original species due to the coordination of the lithium-ions with the amide bond, as depicted in the inset.

Supporting Information), while the LUMO is mostly located on the central thiophene moiety and the amide-bond. The HOMO energy level was theoretically estimated using the empirically obtained procedure published by Chi et al.,<sup>[24]</sup> and shows for EDOT-Amide-TPA a HOMO energy level of  $-5.30$  eV, which is in excellent agreement with our experimentally obtained value.

The electrochemical surface potential (Figure 1e) reveals the electronegative character of the oxygens in the amide-bond, while the most electropositive part is located on the cyclic ether of the EDOT core, resulting in a dipole in the central moiety of the molecule. This dipole, combined with the amide-bond facilitating hydrogen bonding, is anticipated to enable a close molecular packing.<sup>[17]</sup>

## 5. Charge Transport Measurements

Although charge transport in small molecules relies on intermolecular charge transport, charge delocalization within the small molecules is generally considered important.<sup>[25]</sup> As the amide bond is not conjugated, materials with amide bonds in the backbone are generally believed to exhibit poor charge transporting properties in the bulk.<sup>[16]</sup> In order to study the potential of EDOT-Amide-TPA as a HTM for organic electronics, the charge transporting properties were thoroughly characterized.

For the hole mobility measurements, “hole-only” devices were prepared using the following device architecture: indium-doped tin oxide (ITO)/MoO<sub>x</sub>/EDOT-Amide-TPA/MoO<sub>x</sub>/Au.<sup>[26]</sup> *JV*-curves were recorded, with the current assumed to be space-charge limited at higher voltages (Figure S10, Supporting Information). From this, the charge carrier mobility can be estimated using the Mott–Gurney equation.<sup>[26]</sup> The obtained mobility is  $3.9 \times 10^{-5}$  cm<sup>2</sup> V<sup>-1</sup> s<sup>-1</sup> for EDOT-Amide-TPA, which is comparable to that of Spiro-OMeTAD ( $4.0 \times 10^{-5}$  cm<sup>2</sup> V<sup>-1</sup> s<sup>-1</sup>). Upon addition of LiTFSI to the HTM, we observe a significant increase in the mobility to  $2.1 \times 10^{-4}$  cm<sup>2</sup> V<sup>-1</sup> s<sup>-1</sup>, which is ascribed to the reduction of the barrier height for charge hopping.<sup>[27]</sup>

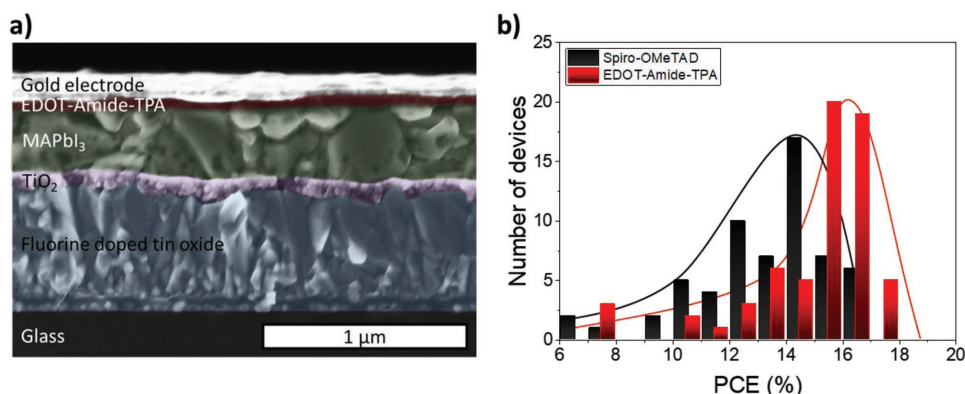
The unexpectedly high hole mobility for EDOT-Amide-TPA was confirmed by using it as the active layer in bottom-gate, bottom-contact organic field effect transistors (OFETs,

Figure S11, Supporting Information). With this technique, the hole mobility for EDOT-Amide-TPA and Spiro-OMeTAD were found to be comparable, confirming the good charge carrier mobility for the nonconjugated EDOT-Amide-TPA.

Besides the charge carrier mobility, conductivity is an important measure for the charge transporting properties. We thus performed in-plane conductivity measurements (Figure 3a, inset) with and without LiTFSI as additive. Upon increasing the concentration of LiTFSI in the HTM solution, the conductivity of EDOT-Amide-TPA films increases spectacularly as shown in Figure 3a, reaching a value of  $1.9 \times 10^{-3}$  S cm<sup>-1</sup> when 300 mol% LiTFSI was added to the solution. We note that, based on the area under the peaks in the optical absorption measurements, the amount of added LiTFSI does not directly correlate to the amount of oxidized species formed (Figure S12, Supporting Information). In contrast, the conductivity in Spiro-OMeTAD has been reported to reach a maximum of  $3 \times 10^{-5}$  S cm<sup>-1</sup> upon addition of 20% LiTFSI, which is significantly lower.<sup>[28]</sup>

This thorough characterization of the charge transporting properties reveals that despite the anticipated poor intramolecular conjugation, EDOT-Amide-TPA shows excellent charge transporting properties that are at least as good as state-of-the-art reference materials such as Spiro-OMeTAD and its conjugated analogues (Table S3, Supporting Information). This also indicates that intramolecular charge delocalization plays a minor role when it comes to facilitating bulk charge transport, which significantly broadens the horizon for the design of new HTMs.

Optical absorption measurements upon addition of LiTFSI reveal the formation of the oxidized species of the HTM (features at 700–800 nm), typical for most oxidized HTMs, and an additional shift of the original absorption peak around 400–440 nm (Figure 3b). The shift of the absorption maximum between the pristine film and the films containing LiTFSI is attributed to the coordination of the Li-ion to the amide-bond (inset Figure 3b), and was confirmed by infrared measurements (Figure S13, Supporting Information). The coordination leads to an increased conjugation through the amide bond, explaining the observed red-shift. It is likely that besides catalyzing the formation of the oxidized species, Li-coordination



**Figure 4.** Photovoltaic performance of MAPbI<sub>3</sub> perovskite solar cells comprising EDOT-Amide-TPA and Spiro-OMeTAD as HTM. a) SEM cross-section of a full device with the following architecture: FTO/compact TiO<sub>2</sub>/MAPbI<sub>3</sub>/EDOT-Amide-TPA/Au. b) Statistical evaluation of 128 individual devices prepared in different batches, comparing the power conversion efficiency of devices comprising either EDOT-Amide-TPA or Spiro-OMeTAD as HTM.

plays a role in the increased conductivity. Furthermore, this interaction increases the solubility of EDOT-Amide-TPA, thus enhancing the processability of the material. The improved solubility upon addition of lithium salts is well-known for amide-based materials and originates from the coordination of the lithium to the amide-bond which competes with the formation of hydrogen bonds (Figure S13, Supporting Information).<sup>[29–31]</sup>

## 6. Device Characterization

As high quality HTM films are required to obtain reproducible devices, the deposition of EDOT-Amide-TPA was optimized. Comparing films of EDOT-Amide-TPA and Spiro-OMeTAD shows that the Spiro-OMeTAD layers often has inhomogeneities (commonly referred to as asteroids) in the film, while this was significantly less apparent in the case of the EDOT-Amide-TPA films (Figure S16b, Supporting Information).

The photovoltaic performance of EDOT-Amide-TPA as a charge extraction material was studied in planar methylammonium lead iodide (MAPbI<sub>3</sub>) perovskite solar cells (fluorinated tin oxide (FTO)/compact TiO<sub>2</sub>/MAPbI<sub>3</sub>/EDOT-Amide-TPA/Au, **Figure 4a**). As perovskite photovoltaic cells often show significant batch-to-batch differences, several batches with a total of 128 individual devices were prepared to compare the photovoltaic performance between EDOT-Amide-TPA and Spiro-OMeTAD (Figure 4b; Figures S14 and S15, Supporting Information). This large dataset allows us to carefully compare the photovoltaic performance and to analyze the results using the *t*-test assuming unequal variance (Table S5, Supporting Information). The statistical analysis shows that the increases in PCE, *V*<sub>oc</sub> and *J*<sub>sc</sub> are significant, while the increase in FF cannot be considered significant from this data set.

The higher open-circuit voltage is an especially important improvement, as it reaches up to 1.12 V for devices comprising EDOT-Amide-TPA, while devices with Spiro-OMeTAD did not exceed 1.08 V. The superior *V*<sub>oc</sub> might be related to the slightly deeper HOMO energy level of EDOT-Amide-TPA.

Despite the significantly thinner HTM layer for EDOT-Amide-TPA (50 nm, Figure 4a), we find the distribution of PCE values to be narrower with this HTM. This demonstrates the

superior film forming properties of our material over Spiro-OMeTAD, for which the reduction of the film thickness results in a significant increase of shunted devices. 50 nm thick layers are achievable in large scale applications, as has been demonstrated for other commonly used materials, i.e., PEDOT:PSS, P3HT, PTAA, PCBM.<sup>[32]</sup> Additionally, a thinner HTM film minimizes the series resistance and also reduces the cost contribution of the HTM when employed in devices.

Recently, perovskites containing mixed halides and cations have been reported to outperform MAPbI<sub>3</sub> when applied in photovoltaic devices.<sup>[33]</sup> As these mixed-perovskites have been quickly adopted by the community, we additionally tested EDOT-Amide-TPA in combination with two of these state-of-the-art alternatives to MAPbI<sub>3</sub>, namely: (FA<sub>0.79</sub>MA<sub>0.16</sub>Cs<sub>0.05</sub>)Pb(I<sub>0.83</sub>Br<sub>0.17</sub>)<sub>3</sub> (FAMACs) and FA<sub>0.83</sub>Cs<sub>0.17</sub>Pb(I<sub>0.83</sub>Br<sub>0.17</sub>)<sub>3</sub> (FACs). A significant improvement of the PCEs was also observed with these perovskites. In combination with FAMACs, PCEs up to 20.0% were obtained with EDOT-Amide-TPA and the *V*<sub>oc</sub> reached up to 1.19 V, significantly outperforming Spiro-OMeTAD (Figures S16–19, and Tables S6 and S7, Supporting Information). The best photovoltaic performance was obtained with EDOT-Amide-TPA in combination with FACs serving as the perovskite absorber, showing a PCE of 20.3% (*V*<sub>oc</sub> = 1.16 V; *J*<sub>sc</sub> = 22.7 mA cm<sup>-2</sup>; FF = 77%), combined with a stunning stabilized power output of 20.0% (**Figure 5a,b**; Figures S20 and 21, and Table S8, Supporting Information). In contrast, the champion Spiro-OMeTAD reference device showed a PCE of 19.7% in the *JV*-scan with a stabilized power of 17.0%. The external quantum efficiency spectrum is shown in Figure 5c and gives an integrated current of 21.4 mA cm<sup>-2</sup>, which is in close agreement with the *JV*-scans. The PCE of 20.3%, obtained with EDOT-Amide-TPA as the HTM is among the highest reported PCEs for a (planar) perovskite solar cell using an alternative for Spiro-OMeTAD.<sup>[5,7,20,34]</sup> Furthermore, to the best of our knowledge, the stabilized power output of 20.0% is the highest reported efficiency for a device comprising FA<sub>0.83</sub>Cs<sub>0.17</sub>Pb(I<sub>0.83</sub>Br<sub>0.17</sub>)<sub>3</sub> as the absorber.<sup>[33,35,36]</sup> By exceeding literature values we have demonstrated that EDOT-Amide-TPA truly has the potential to outperform the current state-of-the-art HTMs in combination with different perovskite materials.

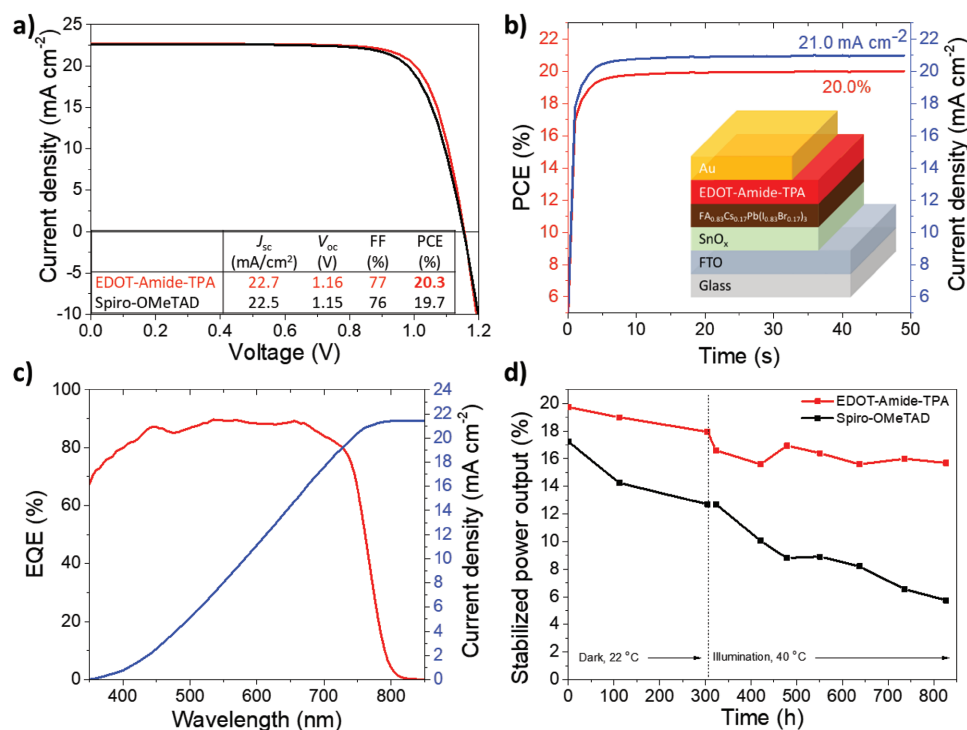


**Figure 5.** Photovoltaic performance and stability of  $\text{FA}_{0.83}\text{Cs}_{0.17}\text{Pb}(\text{I}_{0.83}\text{Br}_{0.17})_3$  perovskite solar cells comprising EDOT-Amide-TPA or Spiro-OMeTAD as HTM. a)  $J$ - $V$ -curves collected under AM 1.5 simulated sunlight of the champion devices comprising EDOT-Amide-TPA and Spiro-OMeTAD in the following device architecture: FTO/SnO<sub>2</sub>/  $\text{FA}_{0.83}\text{Cs}_{0.17}\text{Pb}(\text{I}_{0.83}\text{Br}_{0.17})_3$ /HTM/Au. The photovoltaic parameters are extracted from the  $J$ - $V$ -curves. b) Stabilized power output for the champion device comprising EDOT-Amide-TPA. c) External quantum efficiency with the integrated current. d) Stabilized power output after aging the devices. Initial aging is performed in the dark, followed by testing under illumination at open-circuit at 40 °C. Cells were aged under nitrogen without encapsulation and periodically brought into atmosphere for measurements.

As shown in Figure 4b (Tables S5–S10, Supporting Information), the use of EDOT-Amide-TPA is very reproducible, which we demonstrated by the enhanced performance in several individually prepared batches, using different perovskites. Additionally, we were able to reproduce these results in different labs, and across several batches of EDOT-Amide-TPA.

Excellent performance, low cost and high stability is essential for novel hole transporting materials. In order to study the stability, we performed several stability tests under different conditions on devices without encapsulation, and compared the performance of the devices comprising EDOT-Amide-TPA with Spiro-OMeTAD.

An irradiation aging test was performed at open-circuit under an LED array (Figure S23, Supporting Information), the temperature was controlled at 40 °C in a nitrogen atmosphere. The stabilized power output after 50 s was periodically measured, and is displayed in Figure 5d and Figure S22 (Supporting Information).

Despite the substantially thinner hole transport layer, EDOT-Amide-TPA showed significantly better stability than the devices comprising Spiro-OMeTAD. While the latter showed a pronounced loss in all photovoltaic parameters, no significant loss in the  $J_{sc}$  and FF was observed for devices comprising EDOT-Amide-TPA during the aging experiment (Figures S23 and S24, and Table S11, Supporting Information). We believe that the superior stability of EDOT-Amide-TPA is related to the presence of the amide bonds, as the interactions between

the lithium-ions and the amide bonds facilitate a homogeneous distribution of the ions throughout the HTM layer and minimize their diffusion. In contrast, Lee et al. showed that in Spiro-OMeTAD layers LiTFSI accumulates at the perovskite interface, accelerating the degradation.<sup>[18]</sup> Degradation of the aged devices comprising Spiro-OMeTAD is noticeable, where discoloration can be seen near the electrodes (Figure S25, Supporting Information).

This hypothesis is in good agreement with our 4000 h storage test under inert conditions (Figure S26a, Supporting Information), where devices comprising EDOT-Amide-TPA show a significantly higher PCE than devices comprising Spiro-OMeTAD, while the Spiro-OMeTAD devices additionally show a much broader distribution. In the accelerated thermal stress test, performed at 85 °C (Figure S26d, Supporting Information), EDOT-Amide-TPA devices retain over 90% of their original performance, while Spiro-OMeTAD devices have dropped well below 70% of their original performance and additionally show a broader spread. The superior stability is hypothesized to originate by the suppressed Li-ion migration due to the interaction with the amide bond.

Stability tests performed at different levels of relative humidity were carried out under air (Figure S26b,c, Supporting Information). Although humidity-induced degradation is expected to mostly affect the perovskite, a clear difference is observed between devices comprising EDOT-Amide-TPA and Spiro-OMeTAD. SEM images show the formation of

voids at the Spiro-OMeTAD/perovskite interface (Figure S27, Supporting Information), which is expected to result from moisture induced degradation.<sup>[37,38]</sup> In contrast, no voids or other defects were observed for EDOT-Amide-TPA devices (Figure S27, Supporting Information). The superior stability of devices comprising EDOT-Amide-TPA is expected to originate from the high quality HTM layer that functions as a moisture barrier. This moisture barrier property was recently described for azomethine-based small molecules.<sup>[15]</sup> We additionally show that employing EDOT-Amide-TPA as the HTM leads to improved stability compared to devices comprising Spiro-OMeTAD (Figure S26e, Supporting Information) under the presence of humidity, heat and air.

## 7. Time Resolved Microwave Conductivity (TRMC)

To further investigate the origin of the outstanding performance of EDOT-Amide-TPA we used the TRMC technique, which has been shown to be a powerful technique to investigate the charge injection and recombination dynamics at the perovskite/charge transport layer interface.<sup>[39]</sup> With TRMC, we can measure the time-resolved photo-conductance and hence, gain insights into the mobility and lifetimes of free charges.<sup>[40,41]</sup> Figure 6a shows the photoconductance as a function of time for a neat FAMACs film (blue) and bilayer films consisting of FAMACs combined with EDOT-Amide-TPA (red) or Spiro-OMeTAD (black) (more details can be found Figure S28 of the Supporting Information). The samples are excited at  $\lambda = 430$  nm through the HTM, so that the majority of charge carriers in the perovskite layer are initially generated within 50 nm from the perovskite/HTM interface.<sup>[39]</sup> For the pure FAMACs film, the maximum signal height is close to  $20 \text{ cm}^2 \text{ V}^{-1} \text{ s}^{-1}$ , representing the sum of electron and hole mobilities in the perovskite layer. For the bilayer samples, we note that if holes are extracted by the HTM, these do no longer significantly contribute to the signal as their mobility is only  $\approx 10^{-4} \text{ cm}^2 \text{ V}^{-1} \text{ s}^{-1}$ .<sup>[42]</sup> Therefore, the substantially reduced maximum signal height of  $10 \text{ cm}^2 \text{ V}^{-1} \text{ s}^{-1}$  in the FAMACs/EDOT-Amide-TPA bilayer shows that holes are extracted by the EDOT-Amide-TPA on a sub-ns timescale (i.e., faster than our instrumental response time).<sup>[42]</sup>

Additionally, it suggests that both the electron and hole mobilities in these FAMACs perovskites are about  $10 \text{ cm}^2 \text{ V}^{-1} \text{ s}^{-1}$  and hence, highly balanced.<sup>[41]</sup> This is further confirmed by TRMC experiments in which we illuminated the sample (at  $\lambda = 430$  nm) from the other side, thereby generating the charges several hundred nanometers away from the interface. As shown in Figure 6b, in the case of back side illumination, the sum of electron and hole mobilities is identical to the FAMACs layer, indicating that no charge extraction has occurred on a sub-ns timescale. This can be understood considering that the holes first need to diffuse to the perovskite/EDOT-Amide-TPA interface before these can be extracted. Therefore, the above results show that EDOT-Amide-TPA extracts holes on a sub-ns timescale, provided that the holes are close to the interface. In contrast to the EDOT-Amide-TPA, the maximum signal height in the FAMACs/Spiro-OMeTAD bilayer is the same as for the pure FAMACs, even if charges are excited close to the interface (see Figure 6a and Figure S29 in the Supporting Information). From here, we conclude that extraction of holes from FAMACs by Spiro-OMeTAD is slower than by EDOT-Amide-TPA. These results are in agreement with PL quenching data and lifetime data (Figures S30–32, Supporting Information), and additionally show that the fast hole injection into EDOT-Amide-TPA is not unique to FAMACs perovskites. Fast injection into charge transport layers has been linked to a high  $J_{sc}$  in photovoltaic devices,<sup>[43,44]</sup> explaining the increase in the photocurrent observed for EDOT-Amide-TPA.

## 8. Discussion

What is the origin of the outstanding performance of nonconjugated EDOT-Amide-TPA serving as the HTM in perovskite solar cells? In the following we offer a few possible explanations.

Charge transfer and interfacial recombination at the perovskite/HTM interface most likely plays a crucial role. Time-resolved microwave conductivity measurement performed on perovskite/EDOT-Amide-TPA bilayers show a significantly lower signal amplitude for the perovskite/EDOT-Amide-TPA bilayer suggesting a faster hole injection rate, that has been linked to a high  $J_{sc}$  in photovoltaic devices.<sup>[43,44]</sup>

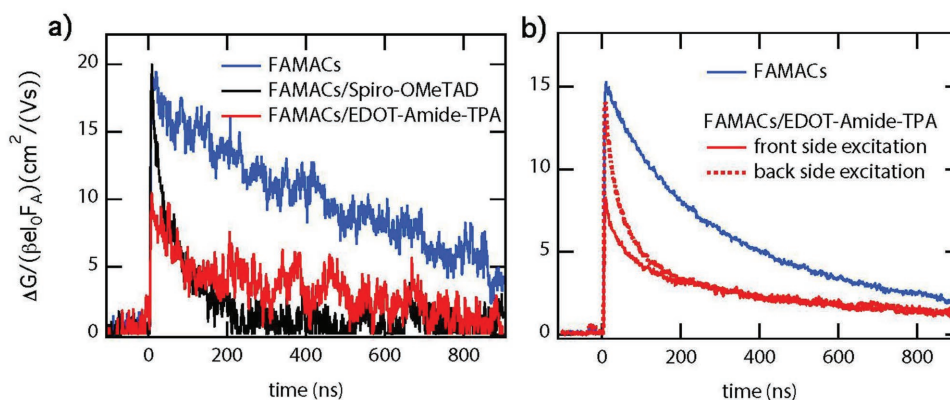


**Figure 6.** Time resolved microwave conductivity traces a) for FAMACs (blue) and the bilayers FAMACs/EDOT-Amide-TPA (red) and FAMACs/Spiro-OMeTAD (black), recorded at  $2 \times 10^{10}$  absorbed photons  $\text{cm}^{-2}$  ( $\lambda = 430$  nm). b) for FAMACs (blue) and FAMACs/EDOT-Amide-TPA (red) illuminated through the HTM (front side, solid line) and through the perovskite (back side, dotted line), at  $2 \times 10^{11}$  absorbed photons  $\text{cm}^{-2}$  ( $\lambda = 430$  nm).

Several publications have shown that the perovskite surface can be passivated using a Lewis base, such as pyridine- or thiophene-based materials.<sup>[5,45,46]</sup> The amide moiety in EDOT-Amide-TPA also behaves like a Lewis base, and therefore a comparable interaction with the perovskite may be expected. This interaction is generally described as a passivation of iodine vacancies, whereby the Lewis base coordinates to the lead and typically results in an enhanced  $V_{oc}$  in devices.<sup>[47,46]</sup> We therefore hypothesize that this surface passivation enhances the effective charge transfer from the perovskite to the HTM and minimizes interfacial recombination in our system, offering an alternative explanation for the observed increase in the  $V_{oc}$ .<sup>[47]</sup> The excellent performance might also be related to a more homogeneous distribution of the LiTFSI dopant throughout the HTM, facilitated by favorable Li-coordination to the amide moiety. When the additives accumulate at the perovskite/HTM interface, they are likely to increase charge recombination and thereby limit the  $V_{oc}$ .<sup>[18]</sup> The accumulation of Li-ions in Spiro-OMeTAD films will be significantly faster, as the ions can diffuse with minimal interaction within the hole transporting layer, leading to the fast degradation of the device.

Furthermore, we propose that a high quality thin HTM layer could play an important role in forming a good interface.<sup>[9]</sup> In this case, the intermolecular interactions between the amide groups assist in the formation of high quality films. Further studies will be required to elucidate the origin of the fast hole injection, the enhanced device stability and the exact role of the amide bond as a functional backbone.

## 9. Conclusions

In summary, we have introduced the amide-functionality in the backbone of HTMs for perovskite solar cells and show that our small-molecule hole conductor, EDOT-Amide-TPA, outperforms state-of-the-art hole-transport material Spiro-OMeTAD when employed as the hole transporting layer in perovskite solar cells. PCEs of up to 20.3% were obtained with a stabilized power output of 20.0%. This stabilized power output is one of the highest reported stabilized efficiencies for HTMs in perovskite solar cells. We show that the improved performance is the result of fast charge injection at the perovskite/EDOT-Amide-TPA interface, as was demonstrated by TRMC measurements. Photovoltaic devices comprising EDOT-Amide-TPA show superior stability which we ascribe to the unique ability of the amide moiety to coordinate with LiTFSI, providing a novel strategy to overcome degradation caused by migration of additives. Here we establish that it is possible for nonconjugated small-molecules to feature charge transporting properties comparable to conjugated materials, indicating that intermolecular charge delocalization can play a dominant role when it comes to facilitating bulk charge transport behavior. By introducing amide bonds, this HTM can be synthesized in a simple condensation reaction that is amenable to scale-up, leading to an estimated material cost of only 5 \$ g<sup>-1</sup>, while this chemistry can also be easily combined with a wide variety of other building blocks. To the best of our knowledge, this is the first demonstration of an HTM with a cost that is at least 10 times lower

than Spiro-OMeTAD and that outperforms state-of-the-art HTMs. Although several efficient HTMs have been published, we believe that the combination of the better performance with a significantly lower cost, higher reproducibility and improved stability makes EDOT-Amide-TPA an ideal candidate to replace Spiro-OMeTAD, and provides the community with a new set of design strategies to develop novel HTMs.

## 10. Experimental Section

**Synthesis of EDOT-Amide-TPA—General Remarks:** All chemicals were purchased from commercial sources and used as received unless stated otherwise. The synthesis was performed under nitrogen atmosphere. 4,4'-Dimethoxy-4''-nitrotriphenylamine (**3**) was synthesized according to literature.<sup>[10]</sup>

**Synthesis of EDOT-Amide-TPA—Synthesis of 3,4-Ethylenedioxythiophene-2,5-dicarbonyl chloride (**2**):** 3,4-Ethylenedioxythiophene-2,5-dicarboxylic acid (**1**) (0.32 g; 1.36 mmol) was dissolved in tetrahydrofuran (THF; 20 mL) and dimethylformamide (DMF; 0.01 mL; 0.14 mmol) was added. Thionyl chloride (SOCl<sub>2</sub>; 0.23 mL, 3.12 mmol) was added dropwise, resulting in a color change to yellow. After heating the solution for 2 h at 80 °C, the solution was allowed to cool down to R.T. and the remaining SOCl<sub>2</sub> and THF were removed under vacuum, resulting in the acid chloride **2** in a quantitative yield, which was used without further purification.

**Synthesis of EDOT-Amide-TPA—Synthesis of N<sup>5</sup>,N<sup>7</sup>-bis(4-(bis(4-methoxyphenyl)amino)phenyl)-2,3-dihydrothieno[3,4-b][1,4]dioxine-5,7-dicarboxamide (EDOT-Amide-TPA):** The total yield of the acid chloride **2** was dissolved in dry THF (20 mL) and 4-amino-4',4''-dimethoxytriphenylamine (**3**) (1 g; 3.12 mmol; 2.3 eq) was added, followed by triethylamine (0.1 mL) which was slowly added to the solution. The dark red solution was heated to reflux for 1.5 h resulting in a bright orange precipitate. The mixture was allowed to cool to R.T. overnight and the orange product was collected *via* filtration and washed with MeOH/Water and THF (yield = 0.99 g; 1.19 mmol; 86%). <sup>1</sup>H-NMR (CDCl<sub>3</sub> + triethylamine to prevent hydrogen bonding; 400 MHz): δ = 8.386 (s, 2 H), 7.396 (d, 4 H, J = 9.2 Hz), 6.992 (d, 8 H, J = 9.2 Hz), 6.918 (d, 4 H, J = 8.8 Hz), 6.797 (d, 8 H, J = 9.2 Hz), 4.542 (s, 4 H), 3.785 (s, 12 H) ppm; <sup>13</sup>C-NMR (CDCl<sub>3</sub> + triethylamine to prevent hydrogen bonding; 101 MHz): δ = 158.18, 155.74, 145.68, 141.24, 138.94, 130.87, 126.17, 121.89, 121.41, 119.16, 114.79, 65.46, 55.64 ppm; <sup>1</sup>H-NMR (DMSO-d<sub>6</sub>; 400 MHz): δ = 9.104 (s, 2 H), 7.490 (d, 4 H, J = 8.8 Hz), 6.969 (d, 8 H, J = 8.8 Hz), 6.894 (d, 8 H, J = 9.2 Hz), 6.819 (d, 4 H, J = 9.2 Hz), 4.540 (s, 4 H), 3.734 (s, 12 H) ppm; <sup>13</sup>C-NMR (DMSO-d<sub>6</sub>; 101 MHz): δ = 157.87, 155.33, 144.81, 140.53, 140.49, 131.07, 125.83, 121.62, 120.86, 116.28, 114.89, 65.33, 55.23 ppm; FTIR: ν(cm<sup>-1</sup>): 3374 (w), 2834 (vw), 1663 (m), 1600 (m), 1537 (m), 1501 (vs), 1462 (m), 1443 (w), 1372 (w), 1313 (s), 1285 (s), 1234 (vs), 1094 (s), 1032 (m), 822 (s) 748 (m); HRMS (ESI<sup>+</sup>): *m/z* calcd for C<sub>48</sub>H<sub>42</sub>N<sub>4</sub>O<sub>8</sub>S<sup>+</sup> [M + H]<sup>+</sup>: 835.27961; found: 835.28076.

**General Characterization Techniques:** UV-vis spectra were recorded using a Perkin Elmer Lambda 1050 spectrometer with an integrating sphere. FTIR were obtained using a Perkin Elmer FT-Infrared Spectrometer Paragon 1000. <sup>1</sup>H- and <sup>13</sup>C-NMR spectra were recorded using a Bruker spectrometer Avance III HD 400 MHz. All spectra were referenced to the solvent (<sup>1</sup>H-NMR: CDCl<sub>3</sub> δ = 7.26 ppm; DMSO-d<sub>6</sub> = 2.50 ppm; <sup>13</sup>C-NMR: CDCl<sub>3</sub> δ = 77.0 ppm; DMSO-d<sub>6</sub> = 39.51 ppm). HRMS measurements were carried out using a Thermo Finnigan LTQ FT Ultra.

**Cyclic Voltammetry (CV):** Cyclic voltammetry experiments were performed using a Metrohm Potentiostat (PGSTAT302N) with platinum working and counter electrode and an Ag/AgCl reference electrode. Experiments were performed in anhydrous and degassed dichloromethane solutions of the hole transporter with 0.1 M tetrabutylammonium hexafluorophosphate (tBuNPF<sub>6</sub>) as electrolyte and a scan rate of 100 mV s<sup>-1</sup>. HOMO levels were calculated according

to literature with the formal potential of the  $\text{Fc}^+/\text{Fc}$  redox positioned at  $-5.1$  eV versus vacuum.

**Thermal Characterization:** TGA was performed using a Netzsch STA 449 C Jupiter under nitrogen atmosphere with a scan rate of  $10^\circ\text{C min}^{-1}$ . DSC was performed under nitrogen atmosphere using a Perkin Elmer DSC8000 at a heating rates in the range of  $10$ – $50^\circ\text{C min}^{-1}$ . Melting behavior was confirmed using a melting point apparatus and Leica DMLM optical microscope equipped with crossed polars and a Linkham hot stage.

**X-Ray Diffraction:** X-ray diffraction analysis of HTM crystal structures was carried out in reflection mode using a Bruker D8 Discover diffractometer with Ni-filtered  $\text{Cu K}\alpha_1$ -radiation ( $\lambda = 1.5406 \text{ \AA}$ ) and a position-sensitive semiconductor detector (LynxEye).

**Preparation FACs and FAMACs Devices on  $\text{SnO}_x$ —Substrate Etching and Cleaning:** All chemicals were purchased from Sigma Aldrich unless stated otherwise. FTO coated glass substrates (Pilkington TEC 7) were patterned and then etched with  $2 \text{ M HCl}$  and zinc powder. Substrates were scrubbed with detergent (2% Hellmanex in water) and then sequentially sonicated for 2 min in acetone, isopropyl alcohol, and nanopure deionized water. The FTO was treated in oxygen plasma for 10 min immediately prior to the spin-coating the electron transporting layer.

**Preparation FACs and FAMACs Devices on  $\text{SnO}_x$ —Tin Oxide Electron-Transport Layer:**  $0.05 \text{ M}$  tin (IV) chloride pentahydrate ( $\text{SnCl}_4 \cdot 5\text{H}_2\text{O}$ ) was dissolved in 2-propanol and stirred for 30 min. The solution was spin-coated onto an FTO/glass substrate at 3000 rpm for 30 s. Substrates were dried at  $100^\circ\text{C}$  for 10 min and then annealed at  $180^\circ\text{C}$  for 60 min. Substrates were then treated with a chemical bath deposition.  $1.25 \text{ g}$  urea was dissolved in 100 mL nanopure deionized water.  $25 \mu\text{L}$  of 3-mercaptopropionic acid (99%, Alfa Aesar) and  $1.25 \text{ mL HCl}$  (37%, Alfa Aesar) were added, and the solution was stirred vigorously for 2 min. The substrates were covered in the solution and placed in an oven at  $70^\circ\text{C}$  for 3 h. Finally, the substrates were sonicated in deionized water for 2 min and then annealed again at  $180^\circ\text{C}$  for 60 min. The substrates were treated with UV-ozone for 15 min immediately prior to perovskite deposition. All  $\text{SnO}_x$ -based devices contain 8 pixels per substrate.

**Preparation FACs and FAMACs Devices on  $\text{SnO}_x$ —FACs and FAMACs Perovskite Precursor Solution and Film Deposition:**  $1.45 \text{ M}$   $\text{FA}_{0.83}\text{Cs}_{0.17}\text{Pb}(\text{I}_{0.83}\text{Br}_{0.17})_3$  precursor solution was prepared with 64 mg CsI (Alfa Aesar), 207 mg FAI (Dyesol), 538 mg  $\text{PbI}_2$  (TCI), and 104 mg  $\text{PbBr}_2$  (TCI).  $1.5 \text{ M}$   $\text{Cs}_{0.05}(\text{FA}_{0.83}\text{MA}_{0.17})_{0.95}\text{Pb}(\text{I}_{0.83}\text{Br}_{0.17})_3$  with excess lead iodide was prepared with 215 mg FAI, 28 mg MABr (Dyesol), 634 mg  $\text{PbI}_2$ , and 92 mg  $\text{PbBr}_2$ . A  $1.875 \text{ M}$  solution of CsI in DMSO was then diluted into the precursor solution. Each perovskite solution was prepared in a mixture of anhydrous DMF (800  $\mu\text{L}$ ) and DMSO (200  $\mu\text{L}$ ). The precursor solution was stirred in atmosphere on a hot plate at  $70^\circ\text{C}$  for 15 min. Room temperature precursor solution was deposited on FTO/ $\text{SnO}_2$  substrates in a dry box and spin-coated at 1000 rpm for 10 s and then at 6000 rpm for 35 s (ramp of  $2000 \text{ rpm s}^{-1}$ ). 80  $\mu\text{L}$  of anisole was quickly dispensed onto the substrate 10 s before the end of spin-coating, and then the substrate was annealed on a hot plate at  $100^\circ\text{C}$  for 45 min. The FACs perovskite was deposited at  $\approx 8\%$  relative humidity while the triple cation perovskite was deposited at  $\approx 20\%$  relative humidity.

**Preparation FACs and FAMACs Devices on  $\text{SnO}_x$ —Hole Transport Layer and Electrode Deposition FACs and FAMACs Devices:** The hole transport material (HTM) 2,2',7,7'-tetrakis( $N,N'$ -di-*p*-methoxyphenylamine)-9,9'-spirobifluorene (spiro-OMeTAD) was prepared by dissolving 85 mg spiro-OMeTAD (Lumtec) in 1 mL anhydrous chlorobenzene along with 20  $\mu\text{L}$  lithium bis(trifluoromethanesulfonyl)imide (Li-TFSI) salt in acetonitrile ( $500 \text{ mg mL}^{-1}$ ) and 33  $\mu\text{L}$  *tert*-butylpyridine (tBP). 100  $\mu\text{L}$  of spiro-OMeTAD solution was statically dispensed onto the substrate and then spin-coated at 2000 rpm for 45 s.

EDOT-Amide-TPA solution was prepared with 10 mg of EDOT in 800  $\mu\text{L}$  anhydrous chlorobenzene and 200  $\mu\text{L}$  chloroform along with 10  $\mu\text{L}$  tBP and 20  $\mu\text{L}$  Li-TFSI salt in acetonitrile ( $170 \text{ mg mL}^{-1}$ ). The EDOT-Amide-TPA solution was heated for 5–10 min until the solution

went completely transparent ( $\approx 85^\circ\text{C}$ ), and then passed through a  $0.22 \mu\text{m}$  polytetrafluoroethylene (PTFE) syringe filter while hot. The filtered solution was left on a hot plate at  $75^\circ\text{C}$  while spin-coating. 50  $\mu\text{L}$  EDOT-Amide-TPA solution was quickly dispensed onto the substrates while they were spinning at 1000 rpm for 40 s.

The substrates were left in a desiccator box for 48 h for the HTM to oxidize before thermally evaporating a 50 nm gold electrode under vacuum of  $<7 \times 10^{-6}$  Torr.

**Preparation FACs and FAMACs Devices on  $\text{SnO}_x$ —FACs and FAMACs based Solar Cell Characterization:** Solar cells were measured with an Abet Class AAB solar simulator under simulated AM 1.5 sunlight at  $100 \text{ mW cm}^{-2}$  irradiance, calibrated by a NREL-calibrated KG5 filtered silicon reference cell. A spectral mismatch factor of 1.045 was estimated following a previously established protocol.<sup>[48]</sup> JV curves were recorded with a 2400 Series Sourcemeter by Keithly Instruments. The solar cell were masked with a metal aperture with a defined active area of  $0.0919 \text{ cm}^2$ . Stability measurements under nitrogen for FACs devices were performed in a nitrogen filled glovebox ( $\text{H}_2\text{O}$  and  $\text{O}_2 < 1 \text{ ppm}$ ) under an LED array, with devices held at  $40^\circ\text{C}$ . The unencapsulated devices were periodically taken into atmosphere for 30 min for performance testing. The spectrum of the LED array was collected using a fiber-coupled Ocean Optics MAYAPro spectrometer with a cosine corrector attachment. The measured spectrum of the LED array is shown in Figure S23 (Supporting Information). No correction other than background subtraction has been applied to the measured spectrum.

**Preparation  $\text{MAPbI}_3$  and FAMACs Devices on  $\text{TiO}_x$ —Titanium Oxide Electron-Transport-Layer:**  $2 \text{ M HCl}$  (35  $\mu\text{L}$ ) in anhydrous 2-propanol (2.53 mL) was added dropwise to a solution of titanium isopropoxide (370  $\mu\text{L}$ ) in 2-propanol (2.53 mL) under vigorous stirring. The clear  $\text{TiO}_x$  sol-gel solution was spin-coated dynamically on the FTO substrates at 2000 rpm for 45 s, followed by annealing at  $150^\circ\text{C}$  for 10 min on a hotplate. Finally, the  $\text{TiO}_2$  compact layer, was completed by sintering at  $500^\circ\text{C}$  in air for 45 min, resulting in a 20 nm thick  $\text{TiO}_2$  compact layer and the substrates were cut into pieces of  $3 \times 3 \text{ cm}^2$ . All  $\text{TiO}_x$ -based devices contain 12 pixels per substrate.

**Preparation  $\text{MAPbI}_3$  and FAMACs Devices on  $\text{TiO}_x$ — $\text{MAPbI}_3$  Perovskite Precursor Solution and Film Deposition:** For the  $\text{MAPbI}_3$  precursor solution methylammonium iodide (Dyesol; 0.2 g; 1.25 mmol) and  $\text{PbI}_2$  (TCI,  $>99.997\%$ ; 0.61 g; 1.3 mmol) were dissolved in  $N,N$ -dimethylformamide: dimethyl sulfoxide (DMSO) solvent mixture (1:4 vol/vol; 1 mL) under stirring at  $100^\circ\text{C}$ . The solution was spin-coated dynamically (80  $\mu\text{L}$ ; first at 1000 rpm for 10 s, followed by a second step at 5000 rpm for 30 s) onto the substrate. After 20 s, chlorobenzene (400  $\mu\text{L}$ ) was added on top of the spinning substrate and afterward the substrate was annealed on a hotplate (first at  $40^\circ\text{C}$  for 40 min, followed by a second step at  $100^\circ\text{C}$  for 10 min).

**Preparation  $\text{MAPbI}_3$  and FAMACs Devices on  $\text{TiO}_x$ —FAMACs Perovskite Precursor Solution and Film Deposition:**  $1.5 \text{ M}$   $\text{Cs}_{0.05}(\text{FA}_{0.83}\text{MA}_{0.17})_{0.95}\text{Pb}(\text{I}_{0.83}\text{Br}_{0.17})_3$  with excess lead iodide was prepared with 215 mg FAI, 28 mg MABr (Dyesol), 634 mg  $\text{PbI}_2$  (TCI), and 92 mg  $\text{PbBr}_2$  (TCI). A  $1.875 \text{ M}$  solution of CsI in DMSO was then diluted into the precursor solution. The perovskite solution was prepared in a mixture of anhydrous DMF (800  $\mu\text{L}$ ) and DMSO (200  $\mu\text{L}$ ) and stirred in nitrogen atmosphere on a hot plate at  $70^\circ\text{C}$  for 15 min. After filtration, the room temperature precursor solution was deposited on FTO/ $\text{TiO}_2$  substrates in a nitrogen filled glove box and spin-coated at 1000 rpm for 10 s and then at 6000 rpm for 20 s (ramp of  $2000 \text{ rpm s}^{-1}$ ). 500  $\mu\text{L}$  of chlorobenzene was quickly dispensed onto the substrate 10 s before the end of spin-coating, and then the substrate was annealed on a hot plate at  $100^\circ\text{C}$  for 45 min.

**Preparation  $\text{MAPbI}_3$  and FAMACs Devices on  $\text{TiO}_x$ —Hole Transport Layer and Electrode Deposition:** The hole transporting material spiro-OMeTAD (Boron Chemicals, 99.5% purity) was applied on the perovskite film using a  $75 \text{ mg mL}^{-1}$  solution in chlorobenzene. To this solutions 10  $\mu\text{L mL}^{-1}$  4-*tert*-butylpyridine (tBP) and 30  $\mu\text{L mL}^{-1}$  of a  $170 \text{ mg mL}^{-1}$  bis(trifluoromethane)sulfonamide lithium salt (LiTFSI) solution in acetonitrile were added. For the optimized recipe, EDOT-Amide-TPA was dissolved at  $10 \text{ mg mL}^{-1}$  in a mixture of chlorobenzene: chloroform

(4:1) after the addition of 10  $\mu\text{L mL}^{-1}$  tBP and 20  $\mu\text{L mL}^{-1}$  of the LiTFSI solution (170  $\text{mg mL}^{-1}$ ) at 75 °C (resulting in a clear orange solution). Spiro-OMeTAD was spincoated dynamically at 1500 rpm while EDOT-Amide-TPA was spincoated at 1000 rpm both for 45 s. The devices were stored 48 h under air at room temperature and <30% RH to allow the hole transporting materials to oxidize. The top electrode with a thickness of 40 nm was deposited by thermal evaporation of gold under vacuum (at  $\approx 10^{-7}$  mbar).

**Preparation MAPbI<sub>3</sub> and FAMACs Devices on TiO<sub>x</sub>—MAPbI<sub>3</sub> and FAMACs Based Solar Cell on TiO<sub>x</sub> Characterization:** Current–Voltage (*JV*) characteristics of the perovskite solar cells were measured using a Newport OriolSol 2A solar simulator with a Keithley 2401 source meter. A spectral mismatch factor of 1.002 was estimated following a previously established protocol.<sup>[48]</sup> The devices were illuminated through a shadow mask, yielding an active area of 0.0813  $\text{cm}^2$ . The *JV* curves were recorded under standard AM 1.5G illumination from a xenon lamp, calibrated to a light intensity of 100  $\text{mW cm}^{-2}$  with a Fraunhofer ISE certified silicon diode. The input bias voltage was scanned from  $-1.5$  to 0 V in 0.05 V steps with a rate of 0.2  $\text{V s}^{-1}$ . All prepared devices show a comparable degree of hysteresis between the forward and reverse scan.

**Preparation MAPbI<sub>3</sub> and FAMACs Devices on TiO<sub>x</sub>—External Quantum Efficiency Measurements:** External quantum efficiency (EQE) was measured via custom build Fourier transform photocurrent spectrometer based on a Bruker Vertex 80v Fourier Transform Interferometer. Devices were illuminated with an AM1.5 filtered solar simulator and calibrated with a Newport silicon reference diode with known external quantum efficiency. The devices were masked with a metal aperture with a defined active area of 0.0919  $\text{cm}^2$ .

**Charge Transport Measurements—Hole-Only Device Preparation and Characterization:** ITO-substrates (1.5  $\times$  2.0 cm, VisionTek, 12  $\Omega \text{sq}^{-1}$  to 15  $\Omega \text{sq}^{-1}$ ) were etched and cleaned. The substrates were plasma cleaned prior to the thermal deposition of the MoO<sub>x</sub> layer (10 nm) under vacuum ( $\approx 1 \times 10^{-6}$  mbar). The substrates were exposed to air and stored in a nitrogen-filled glovebox. Next, the EDOT-Amide-TPA was spincoated from chloroform at a concentration of 10  $\text{mg mL}^{-1}$ , for the pristine materials and from a chlorobenzene:chloroform mixture as described above for the films in the presence of the additives. A top electrode of MoO<sub>x</sub> (10 nm), followed by a layer of gold (40 nm) was deposited under vacuum ( $1 \times 10^{-6}$  mbar). The active area of the device was 0.16  $\text{cm}^2$ . Current–voltage characteristics were recorded in air in the dark using a Metrohm potentiostat (PGSTAT302N) at a scan rate of 0.1  $\text{V s}^{-1}$ . The layer thickness, which was around 50 nm, was determined for the individual films by using atomic force microscopy (AFM) measurements, which were performed in tapping mode using a Nanoscope DPN Stage microscope, or with a Veeco Dektak 150.

**Charge Transport Measurements—Organic Field Effect Transistor (OFET) Preparation and Characterization:** OFETs were prepared in a bottom-gate, bottom-contact geometry on n-doped Si wafers (serving as the substrate and gate electrode), coated with 230 nm of thermally grown SiO<sub>2</sub> as the gate dielectric ( $C_i = 15 \text{ nF cm}^{-2}$ ), and photolithographically patterned interdigitated Au (30 nm thick, plus a 10 nm indium-doped tin oxide adhesion layer) source–drain electrodes (Fraunhofer IPMS). The substrates were cleaned sequentially in acetone and then isopropanol for 10 min each in an ultrasonic bath, followed by exposure to oxygen plasma for 10 min. The substrates were then immediately transferred to a nitrogen-filled glovebox for semiconductor deposition. EDOT-Amide-TPA thin-films were deposited by spincoating (speed = 2500 rpm, ramp = 2500  $\text{rpm s}^{-1}$ , time = 45 s) from a 10  $\text{mg mL}^{-1}$  solution in chloroform. Spiro-OMeTAD thin-films were deposited by spincoating (speed = 2500 rpm, ramp = 2500  $\text{rpm s}^{-1}$ , time = 45 s) from a 10  $\text{mg mL}^{-1}$  solution in chlorobenzene. The devices were then quickly transferred to a second glovebox in a parafilm-sealed box for electrical characterization using an Agilent B1500A semiconductor parameter analyzer. Optimal performance was obtained after annealing the devices at 180 °C for 30 min in the glovebox.

**Charge Transport Measurements—Conductivity Device Preparation and Characterization:** Glass substrates with a thin compact layer of

Al<sub>2</sub>O<sub>3</sub> were used to improve the wetting of the HTMs on the substrate. EDOT-Amide-TPA was spincoated at 1000 rpm from chloroform solutions containing the given amount of LiTFSI as oxidant, resulting in a film thickness of  $\approx 50$  nm. The films were allowed to oxidize for 24 h in a desiccator at a relative humidity < 30%. 40 nm thick gold electrodes were thermally deposited under vacuum ( $\approx 10^{-6}$  mbar). The electrode pattern was designed for two point probe measurements with a channel length of 250, 500, and 1000  $\mu\text{m}$ , and a channel width of 0.2, 0.1, and 0.056 m, respectively. No significant differences were observed depending on the electrode pattern and the measured values were averaged over at least 8 individual devices. *JV*-curves were recorded under ambient conditions without illumination using a Keithley 2400 source meter at a scan rate of 1  $\text{V s}^{-1}$  in the range from  $-5$  to 5 V.

**Charge Transport Measurements—Time Resolved Microwave Conductivity:** The MAPbI<sub>3</sub> and FAMACs films with and without the HTM layer on top were spin-coated on quartz substrates using the same procedure as for the solar cell devices. The thin films on quartz substrates were placed in a sealed microwave cell inside an N<sub>2</sub>-filled glovebox. The TRMC technique was used to measure the change in microwave (8.5 GHz) power after pulsed excitation (repetition rate 10 Hz) of the samples at different excitation wavelengths.<sup>[40]</sup> The bilayers were illuminated from the front side (through the HTM layer) or the back side. For bilayers comprising EDOT-Amide-TPA that have been excited through the HTM, the intensity has been corrected for the parasitic absorption of the HTM at 430 nm.

**Charge Transport Measurements—Computational Study:** The geometry optimization and electronic structure calculations were carried out using Gaussian09 program package. DFT geometry optimizations using the B3LYP/6-31G(d,p) basis set were performed in vacuum and in dichloromethane as the solvent, by means of the conductor-like polarizable continuum model (CPCM). The calculated HOMO energy level was obtained by adding 0.624 eV to the HOMO energy level obtained from DFT calculations using DCM as solvent.<sup>[24]</sup>

## Supporting Information

Supporting Information is available from the Wiley Online Library or from the author.

## Acknowledgements

The authors acknowledge Dr. Steffen Schmidt for the SEM images. This project was financed by a grant from the Federal Ministry of Education and Research (BMBF) under the project ID 03SF0516B. The authors acknowledge funding from the Bavarian Collaborative Research Program “Solar Technologies Go Hybrid” (SolTech), the Center for NanoScience (CeNS), the DFG Excellence Cluster “Nanosystems Initiative Munich” (NIM), the Netherlands Organization for Scientific Research (NWO), and the Marshall Aid Commemoration Commission.

## Conflict of Interest

The authors declare no conflict of interest.

## Keywords

amides, hole transporting materials, low-cost, perovskites, solar cells

Received: May 24, 2018

Revised: August 19, 2018

Published online: October 8, 2018

- [1] N. J. Jeon, J. H. Noh, Y. C. Kim, W. S. Yang, S. Ryu, S. Il Seok, *Nat. Mater.* **2014**, *13*, 897.
- [2] A. Kojima, K. Teshima, Y. Shirai, T. Miyasaka, *J. Am. Chem. Soc.* **2009**, *131*, 6050.
- [3] M. L. Petrus, J. Schlipf, C. Li, T. P. Gujar, N. Giesbrecht, P. Müller-Buschbaum, M. Thelakkat, T. Bein, S. Hüttner, P. Docampo, *Adv. Energy Mater.* **2017**, *7*, 1700264.
- [4] N. Arora, M. I. Dar, A. Hinderhofer, N. Pellet, F. Schreiber, S. M. Zakeeruddin, M. Grätzel, *Science* **2017**, *358*, 768.
- [5] M. Saliba, S. Orlandi, T. Matsui, S. Aghazada, M. Cavazzini, J.-P. Correa-Baena, P. Gao, R. Scopelliti, E. Mosconi, K.-H. Dahmen, F. De Angelis, A. Abate, A. Hagfeldt, G. Pozzi, M. Graetzel, M. K. Nazeeruddin, *Nat. Energy* **2016**, *1*, 15017.
- [6] K. Rakstys, S. Paek, P. Gao, P. Gratia, T. Marszalek, G. Grancini, K. T. Cho, K. Genevicius, V. Jankauskas, W. Pisula, M. K. Nazeeruddin, *J. Mater. Chem. A* **2017**, *5*, 7811.
- [7] D. Bi, B. Xu, P. Gao, L. Sun, M. Grätzel, A. Hagfeldt, *Nano Energy* **2016**, *23*, 138.
- [8] A. Binek, M. L. Petrus, N. Huber, H. Bristow, Y. Hu, T. Bein, P. Docampo, *ACS Appl. Mater. Interfaces* **2016**, *8*, 12881.
- [9] L. K. Ono, S. R. Raga, M. Remeika, A. J. Winchester, A. Gabe, Y. Qi, *J. Mater. Chem. A* **2015**, *3*, 15451.
- [10] M. L. Petrus, T. Bein, T. J. Dingemans, P. Docampo, *J. Mater. Chem. A* **2015**, *3*, 12159.
- [11] J. C. Hindson, B. Ulgut, R. H. Friend, N. C. Greenham, B. Norder, A. Kotlewski, T. J. Dingemans, *J. Mater. Chem.* **2010**, *20*, 937.
- [12] M. L. Petrus, M. Sirtl, A. C. Closs, T. Bein, P. Docampo, *Mol. Syst. Des. Eng.* **2018**, <https://doi.org/10.1039/C8ME00023A>.
- [13] M. L. Petrus, R. K. M. Bouwer, U. Lafont, S. Athanasopoulos, N. C. Greenham, T. J. Dingemans, *J. Mater. Chem. A* **2014**, *2*, 9474.
- [14] M. Daskeviciene, S. Paek, Z. Wang, T. Malinauskas, G. Jokubauskaite, K. Rakstys, K. T. Cho, A. Magomedov, V. Jankauskas, S. Ahmad, H. J. Snaith, V. Getautis, M. K. Nazeeruddin, *Nano Energy* **2017**, *32*, 551.
- [15] M. L. Petrus, A. Music, A. C. Closs, J. C. Bijleveld, M. T. Sirtl, Y. Hu, T. J. Dingemans, T. Bein, P. Docampo, *J. Mater. Chem. A* **2017**, *5*, 25200.
- [16] C. R. Kemnitz, M. J. Loewen, *J. Am. Chem. Soc.* **2007**, *129*, 2521.
- [17] I. Paraschiv, K. de Lange, M. Giesbers, B. van Lagen, F. C. Grozema, R. D. Abellon, L. D. A. Siebbeles, E. J. R. Sudholter, H. Zuilhof, A. T. M. Marcelis, *J. Mater. Chem.* **2008**, *18*, 5475.
- [18] I. Lee, J. H. Yun, H. J. Son, T.-S. Kim, *ACS Appl. Mater. Interfaces* **2017**, *9*, 7029.
- [19] T. P. Osedach, T. L. Andrew, V. Bulović, *Energy Environ. Sci.* **2013**, *6*, 711.
- [20] T. Malinauskas, M. Saliba, T. Matsui, M. Daskeviciene, S. Urnikaitė, P. Gratia, R. Send, H. Wonneberger, I. Bruder, M. Graetzel, V. Getautis, M. K. Nazeeruddin, *Energy Environ. Sci.* **2016**, *9*, 1681.
- [21] F. Zhang, Z. Wang, H. Zhu, N. Pellet, J. Luo, C. Yi, X. Liu, H. Liu, S. Wang, X. Li, Y. Xiao, S. M. Zakeeruddin, D. Bi, M. Grätzel, *Nano Energy* **2017**, *41*, 469.
- [22] D. Prat, O. Pardigon, H.-W. Flemming, S. Letestu, V. Ducandas, P. Isnard, E. Guntrum, T. Senac, S. Ruisseau, P. Cruciani, P. Hosek, *Org. Process Res. Dev.* **2013**, *17*, 1517.
- [23] J. M. García, F. C. García, F. Serna, J. L. de la Peña, *Prog. Polym. Sci.* **2010**, *35*, 623.
- [24] W.-J. Chi, Q.-S. Li, Z.-S. Li, *Nanoscale* **2016**, *8*, 6146.
- [25] P. Liu, B. Xu, Y. Hua, M. Cheng, K. Aitola, K. Sveinbjörnsson, J. Zhang, G. Boschloo, L. Sun, L. Kloo, *J. Power Sources* **2017**, *344*, 11.
- [26] M. L. Petrus, F. S. F. Morgenstern, A. Sadhanala, R. H. Friend, N. C. Greenham, T. J. Dingemans, *Chem. Mater.* **2015**, *27*, 2990.
- [27] H. J. Snaith, M. Grätzel, *Appl. Phys. Lett.* **2006**, *89*, 262114.
- [28] A. Abate, T. Leijtens, S. Pathak, J. Teuscher, R. Avolio, M. E. Errico, J. Kirkpatrick, J. M. Ball, P. Docampo, I. McPherson, H. J. Snaith, *Phys. Chem. Chem. Phys.* **2013**, *15*, 2572.
- [29] F. C. Grozema, A. S. Best, L. van Eijck, J. Stride, G. J. Kearley, S. W. de Leeuw, S. J. Picken, *J. Phys. Chem. B* **2005**, *109*, 7705.
- [30] D. Balasubramanian, R. Shaikh, *Biopolymers* **1973**, *12*, 1639.
- [31] H. Sigel, R. B. Martin, *Chem. Rev.* **1982**, *82*, 385.
- [32] D. Vak, H. Weerasinghe, J. Ramamurthy, J. Subbiah, M. Brown, D. J. Jones, *Solar Energy Mater. Solar Cells* **2016**, *149*, 154.
- [33] M. Saliba, T. Matsui, J.-Y. Seo, K. Domanski, J.-P. Correa-Baena, M. K. Nazeeruddin, S. M. Zakeeruddin, W. Tress, A. Abate, A. Hagfeldt, M. Grätzel, *Energy Environ. Sci.* **2016**, *9*, 1989.
- [34] B. Xu, J. Zhang, Y. Hua, P. Liu, L. Wang, C. Ruan, Y. Li, G. Boschloo, E. M. J. Johansson, L. Kloo, A. Hagfeldt, A. K.-Y. Jen, L. Sun, *Chem* **2017**, *2*, 676.
- [35] Z. Wang, Q. Lin, F. P. Chmiel, N. Sakai, L. M. Herz, H. J. Snaith, *Nat. Energy* **2017**, *2*, 17135.
- [36] D. P. McMeekin, G. Sadoughi, W. Rehman, G. E. Eperon, M. Saliba, M. T. Hörlantner, A. Haghhighirad, N. Sakai, L. Korte, B. Rech, M. B. Johnston, L. M. Herz, H. J. Snaith, *Science* **2016**, *351*, 151.
- [37] Y. Hu, M. F. Aygüler, M. L. Petrus, T. Bein, P. Docampo, *ACS Energy Lett.* **2017**, *2*, 2212.
- [38] Z. Hawash, L. K. Ono, S. R. Raga, M. V Lee, Y. Qi, *Chem. Mater.* **2015**, *27*, 562.
- [39] E. M. Hutter, J.-J. Hofman, M. L. Petrus, M. Moes, R. D. Abellon, P. Docampo, T. J. Savenije, *Adv. Energy Mater.* **2017**, *7*, 1602349.
- [40] T. J. Savenije, A. J. Ferguson, N. Kopidakis, G. Rumbles, *J. Phys. Chem. C* **2013**, *117*, 24085.
- [41] Y. Hu, E. M. Hutter, P. Rieder, I. Grill, J. Hanisch, M. F. Aygüler, A. G. Hufnagel, M. Handloser, T. Bein, A. Hartschuh, K. Tvingstedt, V. Dyakonov, A. Baumann, T. J. Savenije, M. L. Petrus, P. Docampo, *Adv. Energy Mater.* **2018**, *8*, 1703057.
- [42] C. S. Ponseca, T. J. Savenije, M. Abdellah, K. Zheng, A. Yartsev, T. Pascher, T. Harlang, P. Chabera, T. Pullerits, A. Stepanov, J.-P. Wolf, V. Sundström, *J. Am. Chem. Soc.* **2014**, *136*, 5189.
- [43] J. Jiménez-López, W. Cambarau, L. Cabau, E. Palomares, *Sci. Rep.* **2017**, *7*, 6101.
- [44] J. Zhang, B. Xu, L. Yang, C. Ruan, L. Wang, P. Liu, W. Zhang, N. Vlachopoulos, L. Kloo, G. Boschloo, L. Sun, A. Hagfeldt, E. M. J. Johansson, *Adv. Energy Mater.* **2017**, 1701209.
- [45] H. Zhang, L. Xue, J. Han, Y. Q. Fu, Y. Shen, Z. Zhang, Y. Li, M. Wang, *J. Mater. Chem. A* **2016**, *4*, 8724.
- [46] B. Chaudhary, A. Kulkarni, A. K. Jena, M. Ikegami, Y. Udagawa, H. Kunugita, K. Ema, T. Miyasaka, *ChemSusChem* **2017**, *10*, 2473.
- [47] R. A. Belisle, P. Jain, R. Prasanna, T. Leijtens, M. D. McGehee, *ACS Energy Lett.* **2016**, *1*, 556.
- [48] H. J. Snaith, *Energy Environ. Sci.* **2012**, *5*, 6513.